Thermal instability of a power-law fluid flowing in a horizontal porous layer with an open boundary: a two-dimensional analysis

M. Celli[1]; A. Barletta[1]; S. Longo[2]; L. Chiapponi[2]; V. Ciriello[3]; V. Di Federico[3]; A. Valiani[4]

[1]Department of Industrial Engineering, Alma Mater Studiorum Università di Bologna, Viale Risorgimento 2, 40136 Bologna, Italy.

[2] Department of Engineering and Architecture, Università degli Studi di Parma, Parco Area delle Scienze 181/A, 43124 Parma, Italy.

[3]Department of Civil, Chemical, Environmental, and Materials Engineering, Alma Mater Studiorum Università di Bologna, Viale Risorgimento 2, 40136 Bologna, Italy.

[4]Department of Engineering, Università degli Studi di Ferrara, Via Saragat 1, 44122 Ferrara, Italy.

Abstract

A two-dimensional analysis of the onset of thermal convective instability in a horizontal porous layer with open upper boundary is carried out. The saturating fluid is non-Newtonian of power-law behaviour and its flow is represented through a suitable extension of Darcy's law. A model of temperature-dependent viscosity is employed where the consistency index is considered as variable, while the power-law index is assumed to be constant. Numerical data for the neutral stability and for the critical values of a modified Darcy-Rayleigh number have been obtained. The feasibility of an experimental validation of the theoretical results predicted by the stability analysis is discussed in detail. An experimental setup based on a Hele-Shaw cell is described and preliminary results relative to the onset of convective cells are described. Observed hysteretic effects and deviations from the rheological model are identified as potential sources of uncertainty.

Keywords: Porous medium; Non-Newtonian fluid; Thermal instability; Hele-Shaw cell; Rayleigh number; Particle Image Velocimetry (PIV)

1 Introduction

The Rayleigh-Bénard instability of a saturated porous medium has been widely studied in the last decades (Rees, 2000; Nield and Bejan, 2013). Starting with the pioneering studies of Horton and Rogers (1945) and of Lapwood (1948), the analysis was extended to the case where the saturating fluid undergoes a stationary and parallel horizontal flow (Prats, 1966). It was proved that the horizontal flow does not alter the onset conditions for the thermal instability, which occur when the wave number of the perturbation is π and the Darcy-Rayleigh number is $4\,\pi^2$. A synthesis of the effects of different boundary conditions on the

Rayleigh-Bénard instability in a porous medium was provided by Nield (1968). This author investigated configurations where the porous layer has either impermeable or open boundaries.

It should be mentioned that, while the largest part of the existing literature on this topic is relative to Newtonian fluids saturating porous media, a few papers extended the results reported by Horton and Rogers (1945), Lapwood (1948), and Prats (1966) to non-Newtonian fluids. Some authors studied viscoelastic fluids (Hirata and Ouarzazi, 2010; Delenda et al., 2012), while others were concerned with purely viscous fluids modelled through a power law (Barletta and Nield, 2011; Nield, 2011a,b; Alloui et al., 2012; Alves and Barletta, 2013; Barletta and Storesletten, 2016). A recent study has been published about the Rayleigh-Bénard instability in a porous medium saturated by a Bingham fluid (Rees, 2015).

The aim of this paper is twofold. On the one hand, we further expand the knowledge about onset of thermal instability in a horizontal porous layer saturated by a power-law fluid. Our attention will be focussed on the effects on instability of an open upper boundary and of a temperature-dependent apparent viscosity, thus extending the findings reported in Barletta and Nield (2011) and in Alves and Barletta (2013). On the other hand, we critically discuss the experimental validation of the theoretical result. The design of an apparatus based on a Hele-Shaw cell will be illustrated and some early results concerning the structure of the convection cells will be used as a basis for future developments.

For Newtonian fluids, experimental validation of theoretical models of Rayleigh-Bénard convection in porous media has been pursued via either Hele-Shaw analogues (e.g., Hartline and Lister, 1977; Cherkaoui and Wilcock, 2001; Letelier et al., 2016) or direct simulation, using cells or containers filled with a real porous medium (Buretta and Berman, 1976; Lister, 1990; Howle et al., 1997; Keene and Goldstein, 2015). The different techniques used for detecting the incipient instability are based on shadography, the modification of interference fringes of coherent (laser) light due to variations in the refraction index, thermal flux measurements, the visual observation of smoke lines distorted by the recirculation flow.

On the contrary, there are only few attempts to manage experiments with non-Newtonian fluids (Darbouli et al., 2013), given the added complexity in detecting the proper rheological model and measuring the correct parameters. The fluid motion during the early instability phase is characterized by small values of the shear rate; in this range, the rheometers are less accurate, surface effects can be dominant, and the behaviour of artificial fluids is sometimes markedly different from large shear rates.

In this paper, we illustrate some of the challenges posed by these experiments. Hence, we present the Hele-Shaw device used to simulate the instability, and the technical solutions adopted for a correct monitoring of the process and the detection of the instability. We illustrate results of some preliminary experiments conducted in our installation, which qualitatively confirm our theoretical results. We also highlight that deviations from the linear instability model can be due to the simplification introduced by the power-law rheological model, and to the presence of hysteretic effects.

The structure of the paper is as follows. Section 2 presents the linear stability analysis and the determination of the parameters that identify the threshold for the onset of thermally driven convection. These results are discussed and illustrated graphically in Section 3. Section 4 presents the experimental setup, describes a preliminary set of experiments, and discusses the main experimental challenges. As a by-product of our study, a method to infer the power-law model rheological parameters from measurements

conducted in the Hele-Shaw cell is illustrated in Appendix A.

2 Mathematical model

We consider a horizontal porous layer with height H. The lower boundary plane is assumed to be impermeable and isothermal at temperature $T_0 + \Delta T$, with $\Delta T > 0$. The upper boundary is considered as open and subject to a uniform temperature T_0.

2.1 Governing equations

Let us assume the validity of Darcy's law, generalized for non-Newtonian power-law fluids, and of the Oberbeck-Boussinesq approximation to model the thermal buoyancy force. Then, in a regime of local thermal equilibrium between the fluid and the solid phase, we can write the local mass, momentum and energy balance equations as,

$$\boldsymbol{\nabla} \cdot \boldsymbol{u} = 0, \tag{1a}$$

$$\frac{\mu^*}{K} |\boldsymbol{u}|^{n-1} \boldsymbol{u} = - \boldsymbol{\nabla} p - \rho_0 \, \boldsymbol{g} \, \beta \, (T - T_0) \,, \tag{1b}$$

$$\sigma \frac{\partial T}{\partial t} + \boldsymbol{u} \cdot \boldsymbol{\nabla} T = \varkappa \nabla^2 T. \tag{1c}$$

Here, $\boldsymbol{u}$ is the seepage velocity having Cartesian components (u, v, w), T is the temperature and p is the local difference between the pressure and the hydrostatic pressure, μ^* is the consistency index of the fluid, n is the power-law index, K is the permeability, ρ_0 is the fluid density at the reference temperature T_0, $\boldsymbol{g}$ is the gravitational acceleration, β is the thermal expansion coefficient of the fluid, σ is the ratio between the average volumetric heat capacity of the porous medium and the volumetric heat capacity of the fluid, $\varkappa$ is the average thermal diffusivity of the saturated porous medium.

The boundary conditions can be written as

$$\begin{aligned} y = 0 : &\qquad v = 0, \quad T = T_0 + \Delta T, \\ y = H : &\qquad \frac{\partial v}{\partial y} = 0, \quad T = T_0, \end{aligned} \tag{2}$$

where (x, y, z) are the Cartesian coordinates, with y denoting the vertical axis. Equation (1b) can be expressed in its vorticity formulation by evaluating the curl of both sides of this equation, namely

$$\boldsymbol{\nabla} \times \left(\frac{\mu^*}{K} |\boldsymbol{u}|^{n-1} \boldsymbol{u} \right) = \rho_0 \, g \, \beta \, \boldsymbol{\nabla} \times (T \, \boldsymbol{e}_y) \,, \tag{3}$$

where g is the modulus of the gravitational acceleration and $\boldsymbol{e}_y$ is the unit vector along the y axis.

The consistency index μ^* of the power-law fluid is considered as temperature dependent, $\mu^* = \mu^*(T)$. We will follow Nowak et al. (1982) in assuming a constitutive law for μ^* expressed as

$$\mu^*(T) = \mu_0^* \left[1 + \xi \, (T - T_0) \right]^{-n} , \tag{4}$$

where μ_0^* denotes the value of μ^* at reference temperature T_0, and ξ is a fluid property, with units K^{-1}, expressing the temperature change of the consistency index. On the other hand, the temperature change of the power-law index n is considered as negligible.

Equations (1)-(5) can be written in a dimensionless form by introducing the scaling,

$$\frac{1}{H}\,(x,y,z) \to (x,y,z), \quad \frac{H}{\varkappa}\,\boldsymbol{u} = \frac{H}{\varkappa}\,(u,v,w) \to (u,v,w) = \boldsymbol{u}, \quad \frac{\varkappa}{\sigma H^2}\,t \to t,$$
$$\frac{T-T_0}{\Delta T} \to T, \quad H\,\boldsymbol{\nabla} \to \boldsymbol{\nabla}, \quad H^2\,\nabla^2 \to \nabla^2. \tag{5}$$

Thus, we can write

$$\boldsymbol{\nabla}\cdot\boldsymbol{u} = 0, \tag{6a}$$
$$\boldsymbol{\nabla}\times\left[\eta(T)\,|\boldsymbol{u}|^{n-1}\boldsymbol{u}\right] = Ra\,\boldsymbol{\nabla}\times(T\,\boldsymbol{e}_y)\,, \tag{6b}$$
$$\frac{\partial T}{\partial t} + \boldsymbol{u}\cdot\boldsymbol{\nabla}T = \nabla^2 T, \tag{6c}$$
$$y=0: \qquad v=0, \quad T=1,$$
$$y=1: \qquad \frac{\partial v}{\partial y}=0, \quad T=0. \tag{6d}$$

In Eq. (6b), $\eta(T) = \mu^*/\mu_0^*$, and Ra is the Rayleigh number defined as

$$Ra = \frac{\rho_0\, g\, \beta\, \Delta T\, K\, H^n}{\mu_0^*\, \varkappa^n}. \tag{7}$$

We note that $\eta(T)$ is a positive function of T such that $\eta(0) = 1$.

2.2 Basic solution and stability analysis

A stationary basic solution of Eqs. (6) is

$$u_b = Pe\,F(y)^{-1/n}, \qquad v_b = 0, \qquad w_b = 0, \qquad T_b = 1-y, \tag{8}$$

where $Pe > 0$ is the Péclet number and

$$F(y) = \eta(T_b) = \eta(T_b(y)). \tag{9}$$

The basic flow given by Eqs. (8) and (9) is two-dimensional, lying on the (x,y) plane, so that it can be reproduced experimentally by a suitably designed Hele-Shaw cell. Only the instability triggered by two-dimensional modes of perturbation can be detected by employing experimental observations with the Hele-Shaw cell. With this understanding, we will carry out the linear stability analysis in a purely two-dimensional formulation.

The stability of the basic solution (8) can be studied by defining small-amplitude perturbations, namely

$$(u,v) = (u_b,v_b) + \varepsilon\,(U,V), \quad T = T_b + \varepsilon\,\Theta, \tag{10}$$

where (U,V) is the velocity perturbation, Θ is the temperature perturbation, and ε is the perturbation parameter, such that $|\varepsilon| \ll 1$. Besides the temperature and velocity fields, we have to consider also the perturbation of the dimensionless consistency index, namely

$$\eta(T) = \eta(T_b) + \varepsilon\,\eta'(T_b)\,\Theta = \eta(T_b(y)) + \varepsilon\,\eta'(T_b(y))\,\Theta = F(y) - \varepsilon\,F'(y)\,\Theta, \tag{11}$$

where the primes denote derivatives of a function with respect to its argument. Substitution of Eqs. (8) and (10) and Eq. (11) into Eqs. (6) yields, to $O(\varepsilon)$,

$$\frac{\partial U}{\partial x} + \frac{\partial V}{\partial y} = 0, \tag{12a}$$

$$F(y)^{(2n+1)/n} \left(n \frac{\partial U}{\partial y} - \frac{\partial V}{\partial x} \right) + F(y)^{(n+1)/n} F'(y)\, U$$
$$= Pe \left[F''(y) F(y) - F'(y)^2 \right] \Theta + Pe\, F(y) F'(y) \frac{\partial \Theta}{\partial y} - \lambda\, F(y)^2 \frac{\partial \Theta}{\partial x}, \tag{12b}$$

$$\frac{\partial \Theta}{\partial t} + Pe\, F(y)^{-1/n} \frac{\partial \Theta}{\partial x} - V = \nabla^2 \Theta, \tag{12c}$$

$$y = 0 : \qquad V = 0, \quad \Theta = 0,$$

$$y = 1 : \qquad \frac{\partial V}{\partial y} = 0, \quad \Theta = 0, \tag{12d}$$

where

$$\lambda = \frac{Ra}{Pe^{n-1}}. \tag{13}$$

By defining a streamfunction Ψ, such that

$$U = \frac{\partial \Psi}{\partial y}, \qquad V = -\frac{\partial \Psi}{\partial x}, \tag{14}$$

Eq. (12a) is identically satisfied, while Eqs. (12b)–(12d) can be rewritten as

$$F(y)^{(2n+1)/n} \left(n \frac{\partial^2 \Psi}{\partial y^2} + \frac{\partial^2 \Psi}{\partial x^2} \right) + F(y)^{(n+1)/n} F'(y) \frac{\partial \Psi}{\partial y}$$
$$= Pe \left[F''(y) F(y) - F'(y)^2 \right] \Theta + Pe\, F(y) F'(y) \frac{\partial \Theta}{\partial y} - \lambda\, F(y)^2 \frac{\partial \Theta}{\partial x}, \tag{15a}$$

$$\frac{\partial \Theta}{\partial t} + Pe\, F(y)^{-1/n} \frac{\partial \Theta}{\partial x} + \frac{\partial \Psi}{\partial x} = \nabla^2 \Theta, \tag{15b}$$

$$y = 0 : \qquad \Psi = 0, \quad \Theta = 0,$$

$$y = 1 : \qquad \frac{\partial \Psi}{\partial y} = 0, \quad \Theta = 0. \tag{15c}$$

We now write the perturbations in terms of normal modes, namely

$$\left\{ \begin{array}{c} \Psi(x,y,t) \\ \Theta(x,y,t) \end{array} \right\} = \left\{ \begin{array}{c} f(y) \\ h(y) \end{array} \right\} \exp\left[i\, (\alpha x - \omega t) \right]. \tag{16}$$

Eventually, by employing Eqs. (15) and (16), the eigenvalue stability problem can be written as

$$F(y)^{(2n+1)/n} \left(n\, f'' - \alpha^2 f \right) + F(y)^{(n+1)/n} F'(y)\, f'$$
$$= Pe \left[F''(y) F(y) - F'(y)^2 \right] h + Pe\, F(y) F'(y)\, h' - i\, \alpha\, \lambda\, F(y)^2\, h, \tag{17a}$$

$$h'' - \left[\alpha^2 - i\, \omega + i\, \alpha\, Pe\, F(y)^{-1/n} \right] h = i\, \alpha\, f, \tag{17b}$$

$$y = 0 : \qquad f = 0, \quad h = 0,$$

$$y = 1 : \qquad f' = 0, \quad h = 0. \tag{17c}$$

Up to this point, function $F(y)$ has been left undetermined. In fact, on account of Eqs. (5) and (9), this function reflects the model of temperature-dependent consistency index adopted.

On account of Eqs. (4) and (5), $\eta(T)$ can be expressed as

$$\eta(T) = (1 + \gamma\, Ra\, T)^{-n} = (1 + \gamma\, \lambda\, Pe^{n-1}\, T)^{-n}, \tag{18}$$

where γ is a non-negative dimensionless parameter tuning the departure from a constant consistency index model,

$$\gamma = \frac{\mu_0^*\, \varkappa^n\, \xi}{\rho_0\, g\, \beta\, K\, H^n}. \tag{19}$$

As a consequence of Eqs. (9) and (18), one has

$$F(y) = [1 + \gamma\, Ra\, (1 - y)]^{-n} = \left[1 + \gamma\, \lambda\, Pe^{n-1}\, (1 - y)\right]^{-n}. \tag{20}$$

In fact, Eq. (18) is a non-Newtonian extension of the linear fluidity model for Newtonian fluids employed in previous stability analyses of flow in porous media (Barletta and Nield, 2012; Barletta et al., 2016).

In the limiting case $\gamma \to 0$, Eq. (20) predicts $F(y) = 1$, so that Eqs. (17) are drastically simplified to yield

$$n\, f'' - \alpha^2\, f + i\, \alpha\, \lambda\, h = 0, \tag{21a}$$

$$h'' - \left[\alpha^2 + i\, (\alpha\, Pe - \omega)\right] h - i\, \alpha\, f = 0, \tag{21b}$$

$$y = 0: \qquad f = 0, \quad h = 0, \tag{21c}$$

$$y = 1: \qquad f' = 0, \quad h = 0. \tag{21d}$$

Equations (21a) and (21b) are equivalent to those obtained by Alves and Barletta (2013) for the case of impermeable boundaries. The boundary conditions are obviously different. However, with an argument similar to that employed by Alves and Barletta (2013), it can be proved that Eqs. (21) satisfy the principle of exchange of stabilities. Thus, this eigenvalue problem can be solved for $\omega = \alpha\, Pe$ to obtain the limiting value of λ as a function of α for $\gamma \to 0$. In this limit, Eqs. (21) ensure that $\lambda(\alpha)$ is independent of Pe.

We point out that, in the limiting case $\gamma \to 0$, we have $u_b = Pe$ for every $y \in [0, 1]$. Hence, the physical meaning of the principle of exchange of stabilities is that the dimensionless phase velocity of perturbations, ω/α, coincides with the dimensionless basic flow velocity, $u_b = Pe$. In other words, the dimensionless phase velocity of perturbations is zero in the comoving reference frame, namely in the reference frame moving along the x direction with dimensionless velocity $u_b = Pe$. Things are more complicated when γ is nonzero. In fact, the velocity profile u_b is non-uniform. Nonetheless, one can define an average dimensionless velocity of the basic flow,

$$Pe^* = \int_0^1 u_b\, dy = Pe + \frac{\gamma\lambda}{2}\, Pe^n, \tag{22}$$

where Eqs. (8) and (20) have been used. Then, one may define a comoving reference frame as the reference frame moving along the x direction with dimensionless velocity Pe^*. However, one can prove numerically that the dimensionless phase velocity of perturbations in the comoving reference frame is, in general, nonzero. This means that, in the general case described by Eqs. (17), the principle of exchange of stabilities does not hold.

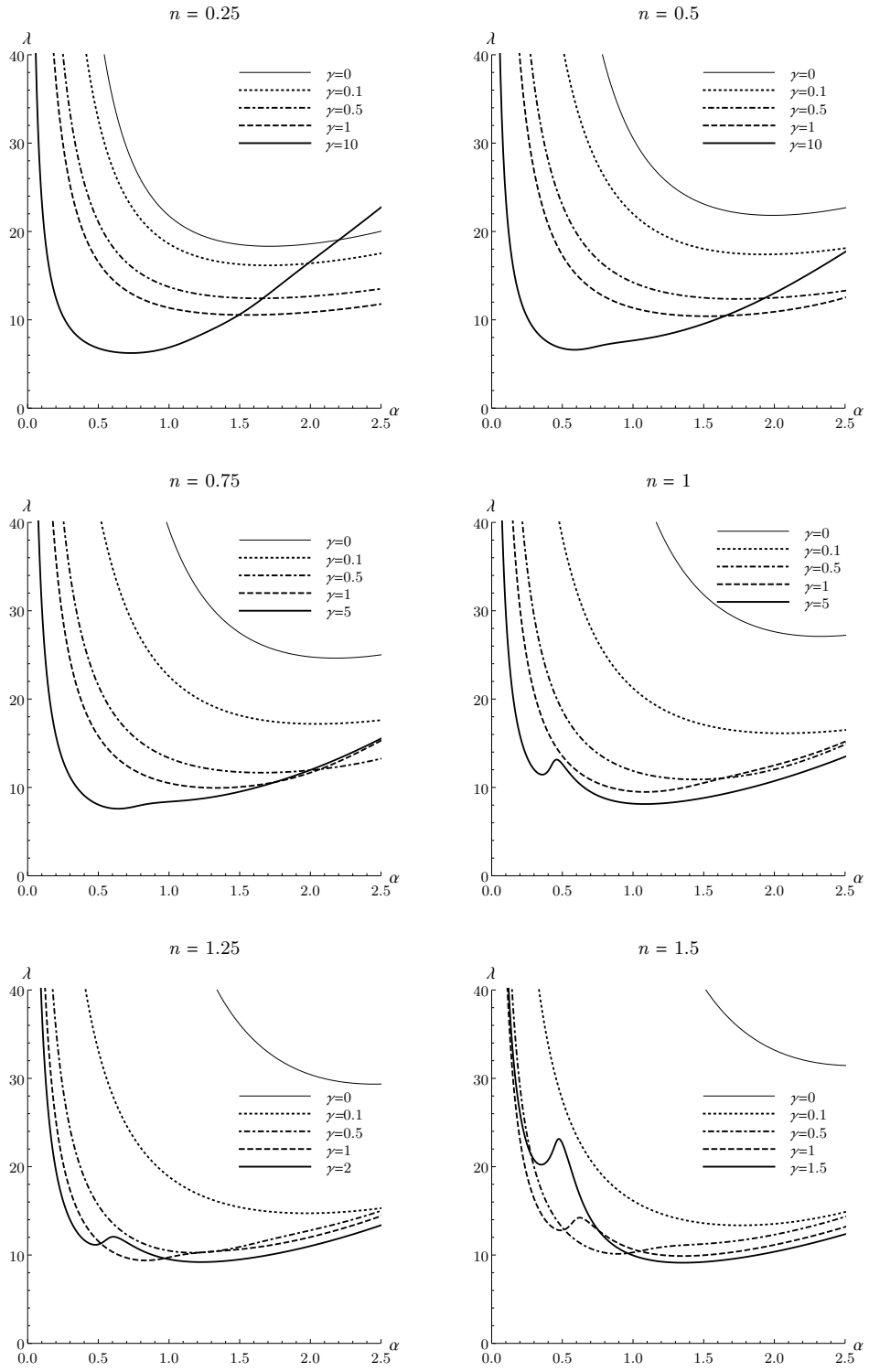

Figure 1: Neutral stability curves for $Pe = 10$ and different values of γ and n

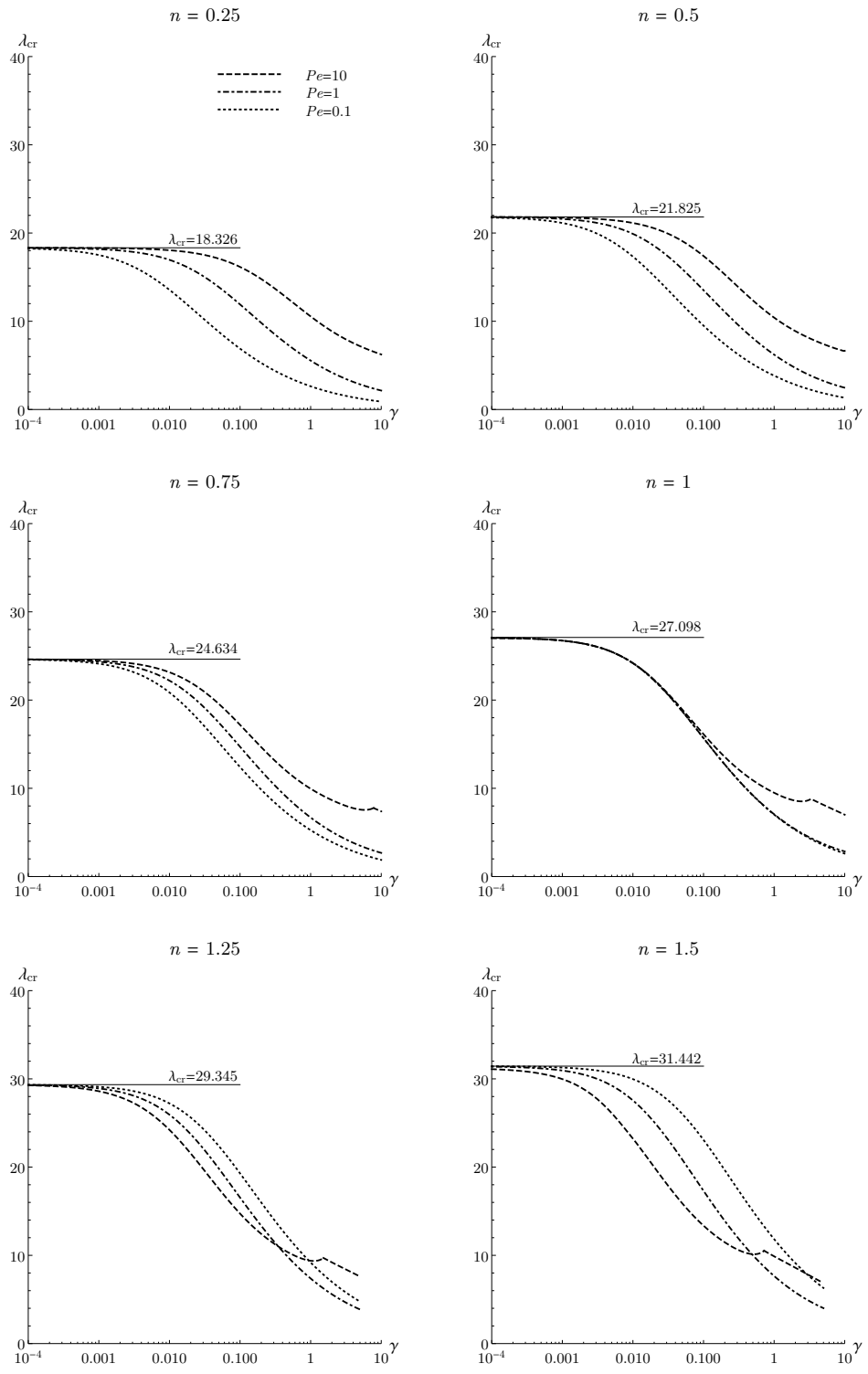

Figure 2: Plots of λ_{cr} as a function of γ, for different values of n and Pe

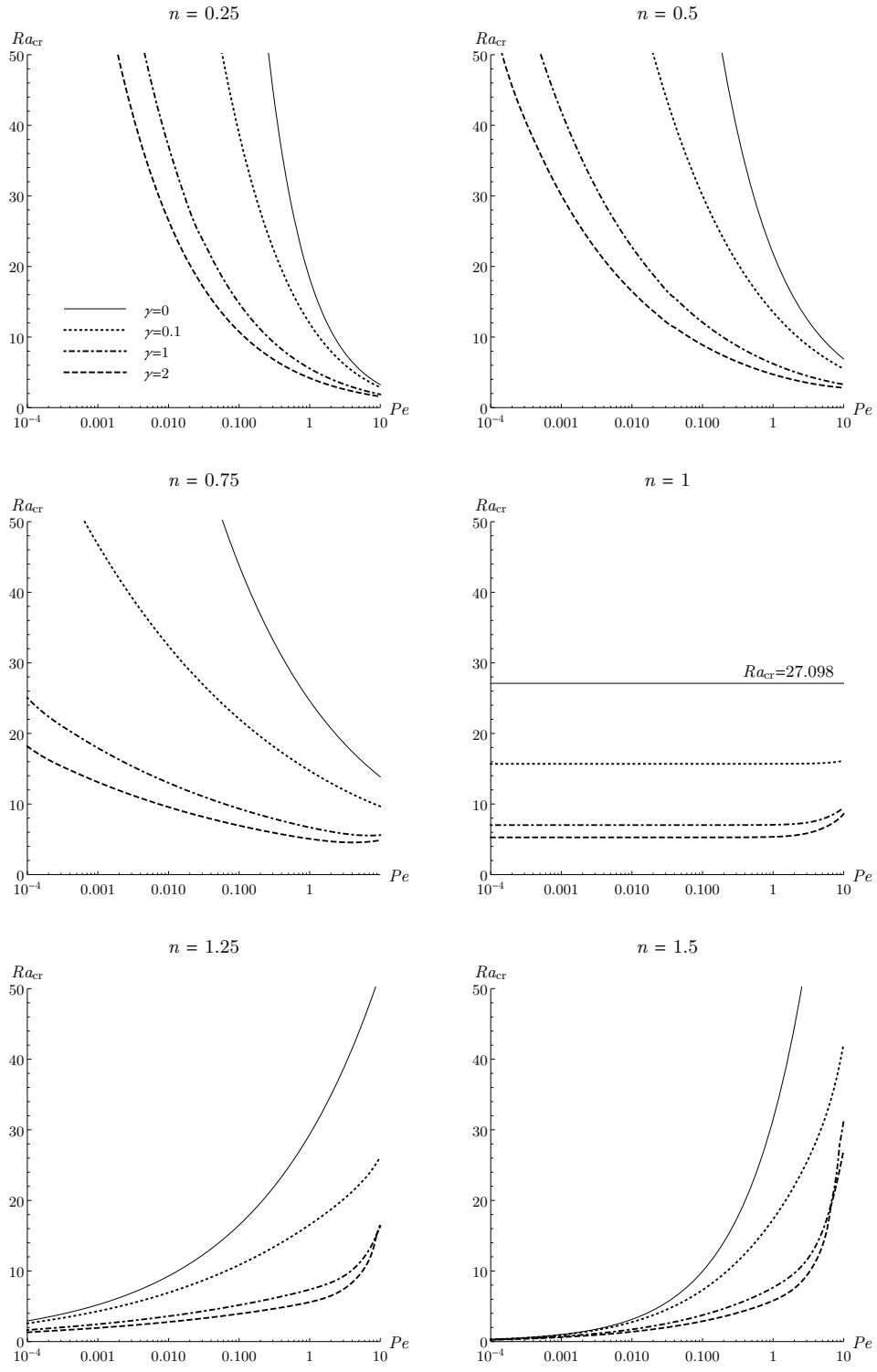

Figure 3: Plots of Ra_{cr} as a function of Pe for different values of γ and n

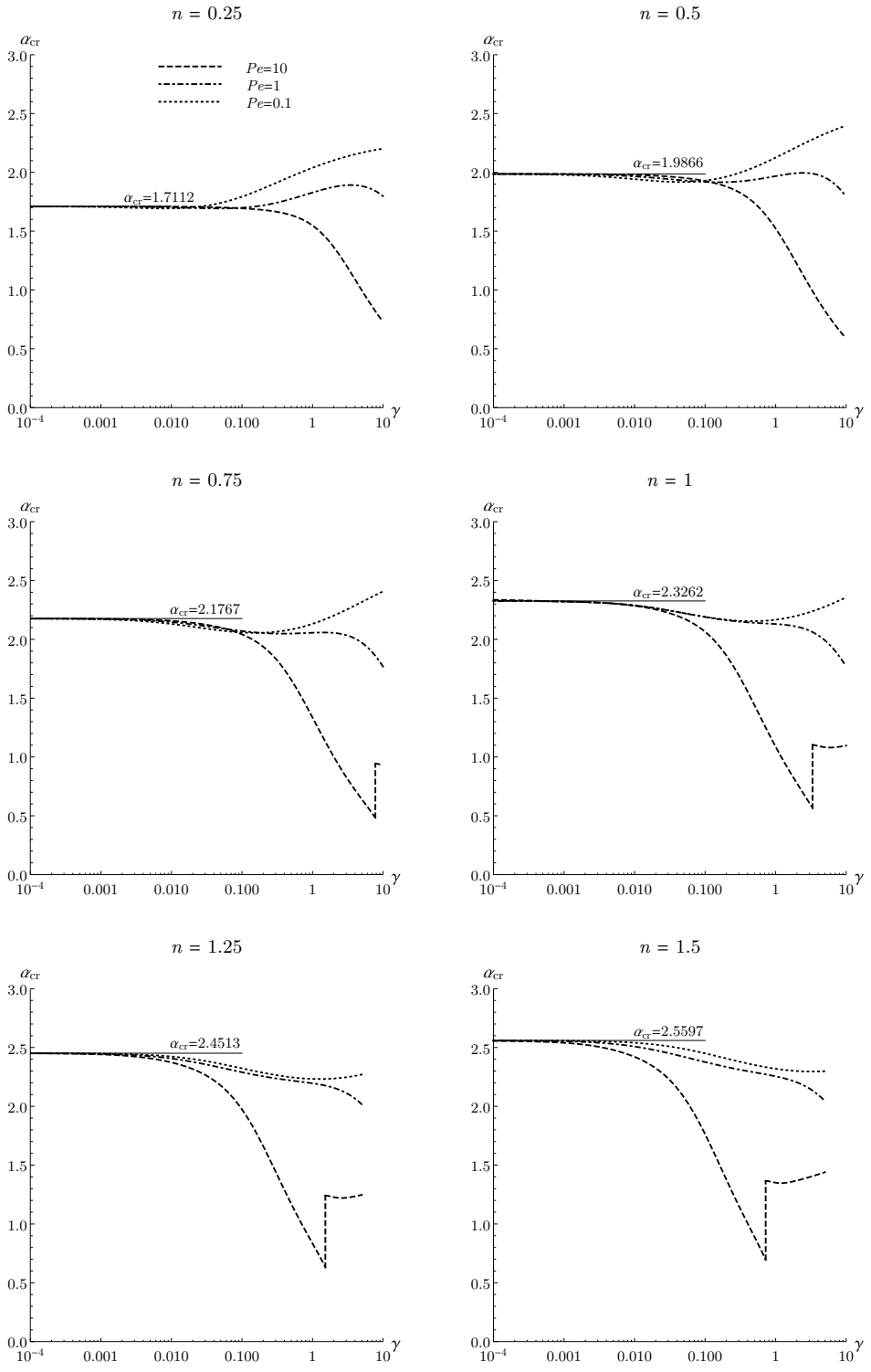

Figure 4: α_{cr} as function of γ for different values of Pe and n

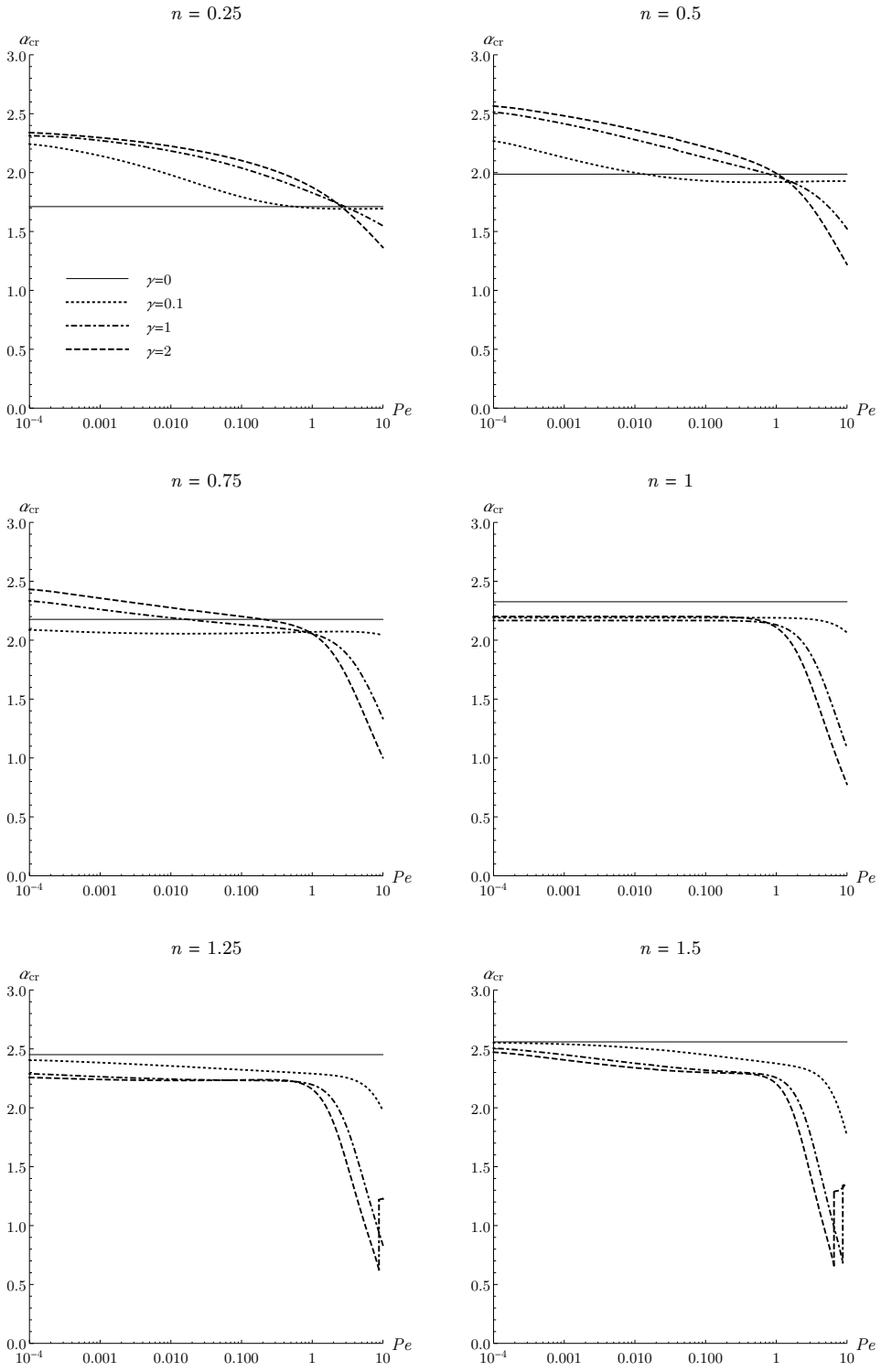

Figure 5: α_{cr} as function of Pe for different values of γ and n

n	α_{cr}	λ_{cr}
0.2	1.63398	17.4558
0.4	1.89159	20.5453
0.6	2.06923	23.0037
0.8	2.20912	25.1486
1.0	2.32621	27.0976
1.2	2.42779	28.9096
1.4	2.51801	30.6186
1.6	2.59952	32.2468
1.8	2.67409	33.8092
2.0	2.74298	35.3168

Table 1: Values of α_{cr} and λ_{cr} as functions of n for the case $\gamma = 0$

2.3 Numerical method

Either Eqs. (17) or Eqs. (21) can be solved numerically. An efficient and accurate procedure is a combined Runge-Kutta solution and shooting method. The Runge-Kutta technique is applied to the system of second-order ordinary differential equations, and the initial conditions are set at $y = 0$,

$$f(0) = 0, \quad f'(0) = 1, \quad h(0) = 0, \quad h'(0) = \chi_1 + i\,\chi_2. \tag{23}$$

A comparison with Eqs. (17) and (21) reveals that there are two extra conditions: $f'(0) = 1$ and $h'(0) = \chi_1 + i\,\chi_2$. The former fixes the undetermined overall scale of the perturbations, while the latter just introduces two unknown real parameters, χ_1 and χ_2. These unknowns, together with ω and λ, are to be determined for prescribed values of (α, n, Pe, γ). The shooting method is employed to evaluate the four real unknowns $(\chi_1, \chi_2, \omega, \lambda)$ by satisfying the target conditions,

$$f'(1) = 0, \quad h(1) = 0. \tag{24}$$

Equations (24) are, in fact, four real equations as f and h are complex functions.

The numerical solution is implemented through the software environment *Mathematica*. In particular, the Runge-Kutta solution is implemented with the built-in function `NDSolve`, while the shooting method is accomplished by using the built-in function `FindRoot`. The default option of `NDSolve`, yielding an adaptive step-size refinement within the interval $0 < y < 1$, is applied. The accuracy of this numerical procedure was tested, with reference to a different eigenvalue problem, in Barletta (2012).

3 Results and discussion

The main purpose of the linear stability analysis is the determination of the values of λ that identify the threshold for the onset of thermally driven convection. These values are the so-called critical values, denoted here by the subscript cr, and they can be identified as the absolute minima of the neutral stability

	α_{cr}			Ra_{cr}			$\omega_{cr} - \alpha_{cr} Pe^*_{cr}$		
γ	$Pe = 0$	$Pe = 0.5$	$Pe = 5$	$Pe = 0$	$Pe = 0.5$	$Pe = 5$	$Pe = 0$	$Pe = 0.5$	$Pe = 5$
10^{-9}	2.32621	2.32621	2.32621	27.0976	27.0976	27.0976	0.00000	0.00000	0.00000
10^{-6}	2.32621	2.32621	2.32621	27.0973	27.0973	27.0973	0.00000	0.00000	0.00002
10^{-4}	2.32572	2.32572	2.32572	27.0604	27.0604	27.0604	0.00000	0.00022	0.00217
10^{-3}	2.32143	2.32143	2.32142	26.7350	26.7350	26.7351	0.00000	0.00212	0.02117
0.01	2.28835	2.28834	2.28757	24.1803	24.1804	24.1857	0.00000	0.01746	0.17472
0.05	2.22275	2.22263	2.21089	18.7226	18.7231	18.7741	0.00000	0.05095	0.51495
0.1	2.19116	2.19082	2.15728	15.6866	15.6877	15.7996	0.00000	0.06667	0.69093
0.5	2.15465	2.15108	1.87073	9.18302	9.18856	9.69731	0.00000	0.04553	1.03011
1	2.16703	2.15759	1.59990	7.01557	7.02589	7.87347	0.00000	−0.02867	1.64535
5	2.28114	2.19879	0.854726	3.54832	3.58811	5.33040	0.00000	−0.55562	10.9945
10	2.36506	2.17148	0.604118	2.59944	2.66738	4.87322	0.00000	−1.02541	21.4352

Table 2: Values of α_{cr}, Ra_{cr} and $\omega_{cr} - \alpha_{cr} Pe^*_{cr}$ as functions of γ for the case $n = 1$ and different values of Pe

curves, $\lambda(\alpha)$. A few examples of these curves are displayed in Fig. 1. This figure is relative to $Pe = 10$. Each frame refers to a different value of n, and each curve is drawn for a different value of γ. One may note that, as the value of n increases, the usual upward-concave shape of the neutral stability curves, typical of Rayleigh-Bénard instability, changes to a doubly-concave shape characterised by two minima. This behaviour occurs for sufficiently high values of both γ, and n. As the neutral stability curves, generally speaking, move down in the (α, λ) plane as γ increases, one may identify an overall destabilising effect of the temperature-dependent apparent viscosity. In the special case of a Newtonian fluid saturating a porous layer, this destabilising effect is a well-known feature (Kassoy and Zebib, 1975; Nield, 1996). In particular, Kassoy and Zebib (1975) pointed out that the lower threshold for thermal instability can be easily explained. In fact, the warmer fluid close to the lower boundary is less viscous than in a constant viscosity model, so that it is more prone to initiate the convective flow.

Figures 2 and 3 display the behaviour of λ_{cr} and Ra_{cr} as functions of the parameters γ and Pe, respectively. Each frame in these figures is drawn for a given value of n. Figure 2 displays plots of $\lambda_{cr}(\gamma)$ for different values of Pe while Fig. 3 displays plots of $\lambda_{cr}(Pe)$ for different values of γ. We point out that, as proved in Section 2.2, the values of λ_{cr} do not depend on Pe in the limiting case $\gamma \to 0$. The solid lines drawn in Fig. 2 indicate the asymptotic behaviour attained when $\gamma \to 0$, obtained by solving Eq. (21). Figure 3 is specially useful as it displays the markedly different trend of Ra_{cr} when Pe becomes smaller and smaller, and either $n < 1$, or $n = 1$, or $n > 1$. This trend suggests that Ra_{cr} increases unboundedly when $n < 1$, approaches a finite non-vanishing limit when $n = 1$, and tends to 0 when $n > 1$. Moreover, Fig. 3 shows that the effect of an increasing Pe is extremely weak for Newtonian fluids, but it is very strong for either pseudoplastic or dilatant fluids. Tables 1 and 2 report values of the critical parameters for the onset of instability in the special cases $\gamma \to 0$ and $n = 1$, respectively. The values reported in Table 1

are independent of Pe as it is made evident from Eqs. (21) and from Figs. 2-5. Table 1 evidences that λ_{cr} undergoes a gradual increase on changing the rheological behaviour of the fluid from pseudoplastic to dilatant, *i.e.* on increasing n. Just the same qualitative behaviour was found for transverse rolls in the case where both boundaries are impermeable (Barletta and Nield, 2011). Table 2 reports (α_{cr}, Ra_{cr}) in the Newtonian case, with different values of Pe. As already mentioned, these data show the destabilising effect of an increasingle variable viscosity. Table 2 reveals that, as γ increases, the data become more and more dependent on the Péclet number. In fact, the pair (α_{cr}, Ra_{cr}) does not depend on Pe when $\gamma \to 0$ and $n = 1$, as it can be inferred from Eqs. (21). Table 2 also reports values of $\omega_{cr} - \alpha_{cr} Pe^*_{cr}$, where Pe^* is defined by Eq. (22). These data show that, at onset of instability, the phase velocity ω_{cr}/α_{cr} is not equal to the basic flow average velocity, Pe^*_{cr}. As already pointed out in Section 2.2, this means that the principle of exchange of stabilities cannot be invoked when $\gamma \neq 0$. An exception illustrated by Table 2 is the case $Pe = 0$ where $\omega_{cr} = 0$.

Figures 4 and 5 display the behaviour of α_{cr} as a function of parameters n, γ, and Pe. Both these figures are made of six frames, each frame being drawn for a given value of n. Figure 4 displays plots of $\alpha_{cr}(\gamma)$ for different values of Pe while Fig. 5 displays plots of $\alpha_{cr}(Pe)$ for different values of γ. The straight solid lines displayed in Fig. 4 yield the values α_{cr} relative to the case $\gamma = 0$.

An interesting feature displayed in Figs. 2-5 is the occurrence of discontinuities in the slope of λ_{cr} associated with jump discontinuities in the trend of α_{cr}. This behaviour is nothing but the consequence of the double-minima shape of the neutral stability curves. When the second minimum of λ versus α becomes the lowest, we observe both the slope discontinuity of λ_{cr} and the jump discontinuity of α_{cr}.

4 Experimental issues

The experimental investigation of the onset of Rayleigh-Bénard cells in non-Newtonian porous flow with an open boundary poses several challenges. First, the adoption of particle tracking or particle image velocimetry (PIV) algorithms to detect the cell growth requires a tracer characterised by a mass density equal to the fluid to prevent sedimentation or flotation, which in turn remove the particles from the fluid and induce perturbations represented by vertical velocities.

Second, the need to establish an average velocity field induces several additional problems. The early stage of cell formation is characterised by an incipient velocity much smaller than the imposed mean velocity, hence it becomes difficult to isolate the velocity induced by thermal convection. The estimation of the average velocity profile, to be subtracted to the flow field in order to isolate the perturbed velocity, should be based, e.g., on a moving time average or a Principal Orthogonal Decomposition (POD), or a filtering of the measured velocity field. All these techniques show an uncertainty much larger than the perturbed velocity itself. Moreover, the presence of an open boundary is a further complication, making the methodology used by Darbouli et al. (2013) to detect the incipient instability inapplicable. In fact, this methodology is based on measuring the thermal flux between the hot and the cold frames against the temperature gradient, as incipient cells enhance the efficiency of thermal transfer. With an open boundary, however, even a modest horizontal velocity field induces variations in the vertical thermal flux much larger

than those generated by the incipient instability.

Finally, experiments with a free surface at the top require the Hele-Shaw cell to be inclined. In fact, the imposed horizontal flow requires a spatial gradient of the free surface, which in turn must be parallel to the bottom and to the top frames. The optimal inclination angle can be obtained by trial-and-error in steady state. However, this regime is never fully reached, and once the cells develop, the overall dissipation increases and the requested spatial gradient increases, making it difficult to adjust the inclination.

These preliminary considerations guided the realization of the experimental setup described below.

4.1 Experimental setup

In order to verify the mechanism of cell formation, a Hele-Shaw cell of length $L = 80$ cm and height $H = 4$ cm was built, similar to Hartline and Lister (1977). The optical access is through two polycarbonate windows 0.8 cm thick, with a gap maintained by aluminium shims of 0.1, 0.2, and 0.3 cm. The assembly is held together by an aluminium frame machined by using a CNC milling cutter. The temperature control is obtained by circulating water at the hot lower side, and coolant at the cold upper side, and modulating the pumps discharge with a Proportional Integral Derivative (PID) control system. The sensors are two PT100 probes, 4 wires AA 1/3DIN with a nominal accuracy of 0.10 K at 0 K, inserted in the upper and in the lower side of the frame. A cross-section and a front view of the Hele-Shaw cell is shown in Figure 6. Note that the upper boundary is not open as in the theoretical model, but impermeable. The sensors were calibrated by comparison with a mercury thermometer of 0.02 K accuracy, the hot sensor in the range $288 - 318$ K and the cold sensor in the range $273 - 303$ K. The sensors showed an excellent linearity, with an estimated maximum uncertainty of 0.08 K in the calibration range. Hence the temperature difference is measured with an expected uncertainty of 0.12 K and can be controlled with the PID within 0.20 K. In order to guarantee a thermal flux in the vertical direction only (from the hot toward the cold frame), the cell is thermally insulated in all its components with foam rubber and thermal insulating tape, leaving a window in correspondence of the polycarbonate plate accessible for velocity measurements. Two free surface tanks, or wells, are connected to the cell, allowing fluid injection and extraction in order to generate a constant flux. A syringe pump is used to inject the requested discharge.

The measurement of velocity is performed with a Particle Image Velocimetry (PIV) system from TSI with a 2048×2048 pixel video camera (TSI Power View Model 630149) fitted with a NIKKOR AF D 50 mm/f lens with an adapter ring (Nikon PK-12). The light source is a water cooled Solo Nd:YAG III dual laser head with a maximum repetition rate of 15 Hz and an output energy of 50 mJ. The laser is mounted on the same side of the video camera, with two cylindrical lenses fitted in order to transform the beam into a spot light instead of the classical sheet of light. The spot light enlightens the accessible window. Polarised filters are added to the video camera to eliminate the reflections. Since the expected velocities are very small, the time interval between the two frames is quite long, but a set up of the synchronyzer with high values of the interval time proved to be unstable. For this reason, we preferred to elaborate frames belonging to different shots, acquired with interval time of the order of seconds. The calibration of the PIV in the experimental configuration gave a resolution of 0.05 mm per pixel. Velocity computation was carried out

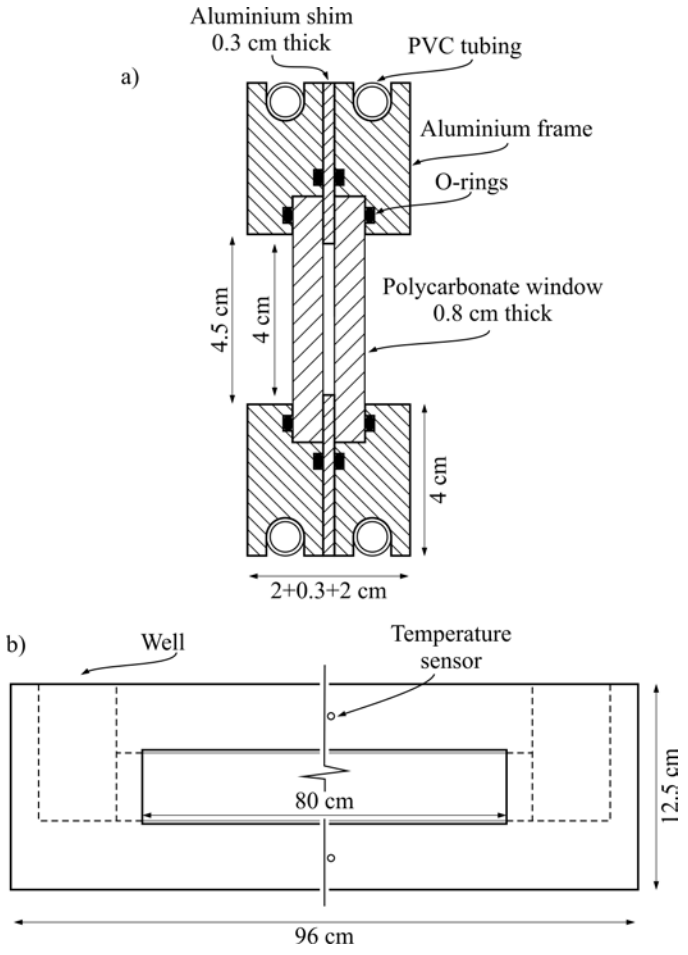

Figure 6: Hele-Shaw cell. (a) Cross section, and (b) front view.

using a Fast Fourier based correlation analysis implemented in a Matlab code (Matpiv 1.6.1 Sveen (2004)). The power law fluid was obtained with two different recipes, by (i) adding Xanthan Gum (XG) with varying concentration (1000 ppm or less) to softened tap water, with added NaCl as a stabilizer, and (ii) adding Carboxymethyl cellulose (CMC) to deionized water and biocide to prevent degradation. Successful mixing was achieved using a low-speed stirrer. Before introducing the fluid in the cell, tracers for PIV were added (Degussa Vestosint® or pine pollen) by using a syringe with several cycles of aspiration and injection in order to improve the homogeneity of the particles distribution.
The rheology of the fluid was measured with a parallel plate rheometer (Dynamic Shear Rheometer Anton Paar Physica MCR 101), and the mass density with a hydrometer (STV3500/23 Salmoiraghi), with an accuracy of 1%.

4.2 Experimental results

Some preliminary test were conducted to check the adequacy of the technique and the overall efficiency of the device. Figure 7 shows four snapshots of the velocity field with increasing temperature gradient from top to bottom. It is seen that recirculation cells with a measured velocity equal to a fraction of one mm/s progressively appear and develop as the temperature gradient increases.

Qualitatively, this is in agreement with the 2-D theoretical model, which predicts that thermal instability for porous flow of a power-law fluid is associated to a non zero Péclet number, i.e., with a non zero horizontal velocity of the fluid. However, preliminary tests conducted in the cell show instability also for a fluid initially at rest. There are two possible reasons for this unexpected behaviour. First, the fluid used in the experiment could have deviated from power-law behaviour at small shear rates. Secondly, the convection cells showed a strong hysteresis effect: the temperature gradient required to trigger convection was decidedly larger than that corresponding to the disappearance of the cells. These nonlinear effects play an important role and demonstrate there is an approximation associated with the linear stability analysis.

Another relevant difficulty was the correct selection of the tracers. In order to have an adequate accuracy in measurements, it is necessary that the tracers follow closely the fluid motion, with a minimal lag and a nearly uniform distribution throughout the flow field; the algorithm for estimating the velocity fails with a limited number of particles. In flow fields with an average non-zero velocity, drag and turbulence mix the tracer particles, counteracting the sedimentation (or floating) due to the action of gravity; in fluids nearly at rest, like in the Hele-Shaw cell of our experiments (at least before the growth of the instabilities), gravity effects are dominant. In order to avoid segregation of the tracers, their mass density should be chosen to be close to the fluid's. However, a major limit is the variability of the mass density of the fluid along the vertical, due to the temperature gradient. The pine pollen particles used in our experiments were partially able to adapt their apparent mass density to the ambient fluid, having a sponge-like structure which favours absorption. However, the particles had an attitude to aggregate, generating lumps which showed a noticeable lag with respect to the fluid motion. In perspective, better results could be obtained using microsponges, presently used in pharmaceutical technology for drug deliver system (Kaity et al., 2010).

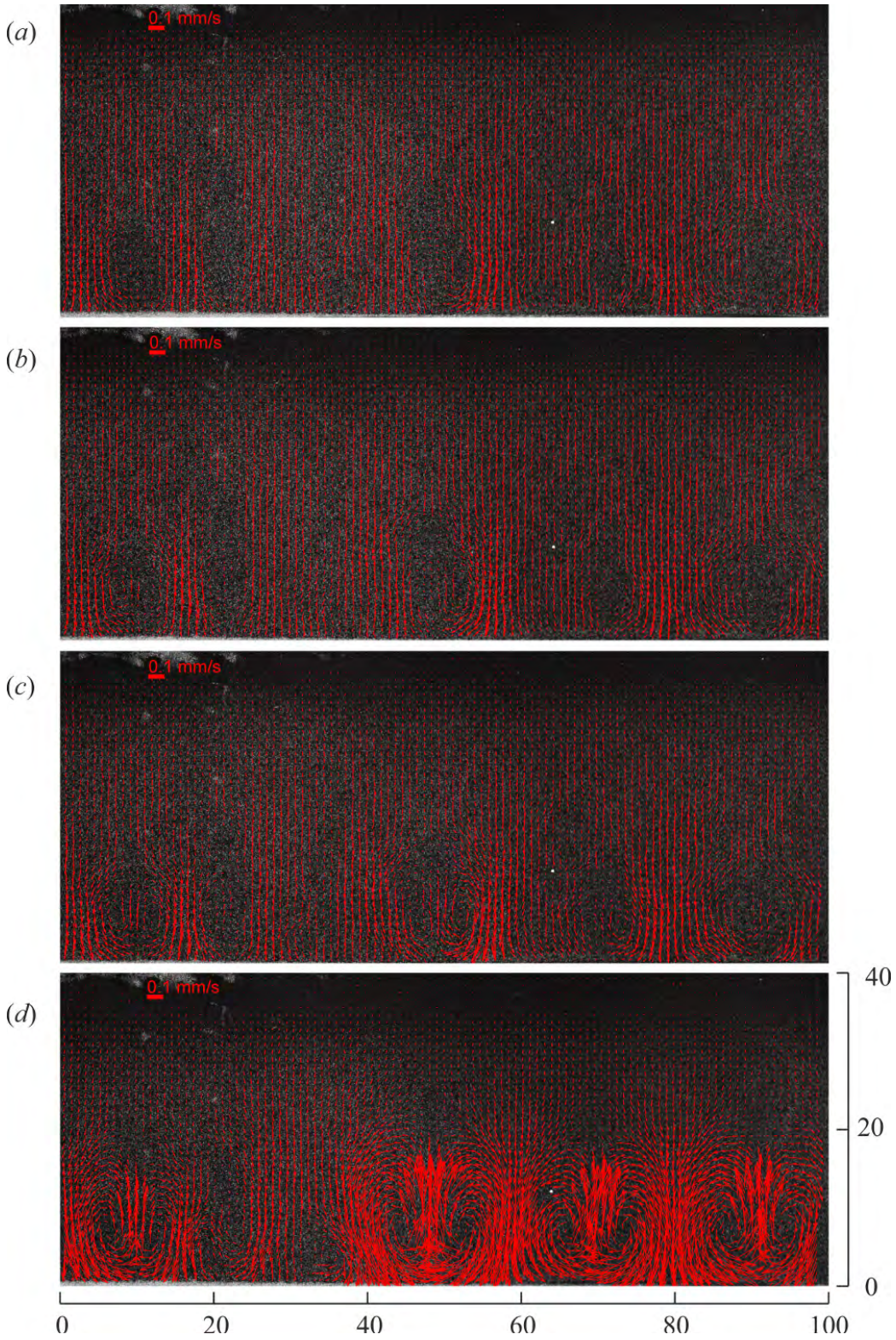

Figure 7: Snapshots of the velocity field measured in the Hele-Shaw cell with a gap thickness of 3 mm. The fluid is shear thinning (water plus CMC 1.5% wgt), with $n = 0.9$ and $\mu_0^* = 0.25$ Pa s^n. (a) $\Delta T = 5.8$ K, (b) $\Delta T = 6.3$ K, (c) $\Delta T = 6.8$ K, (d) $\Delta T = 8.1$ K. The rulers are in millimetres.

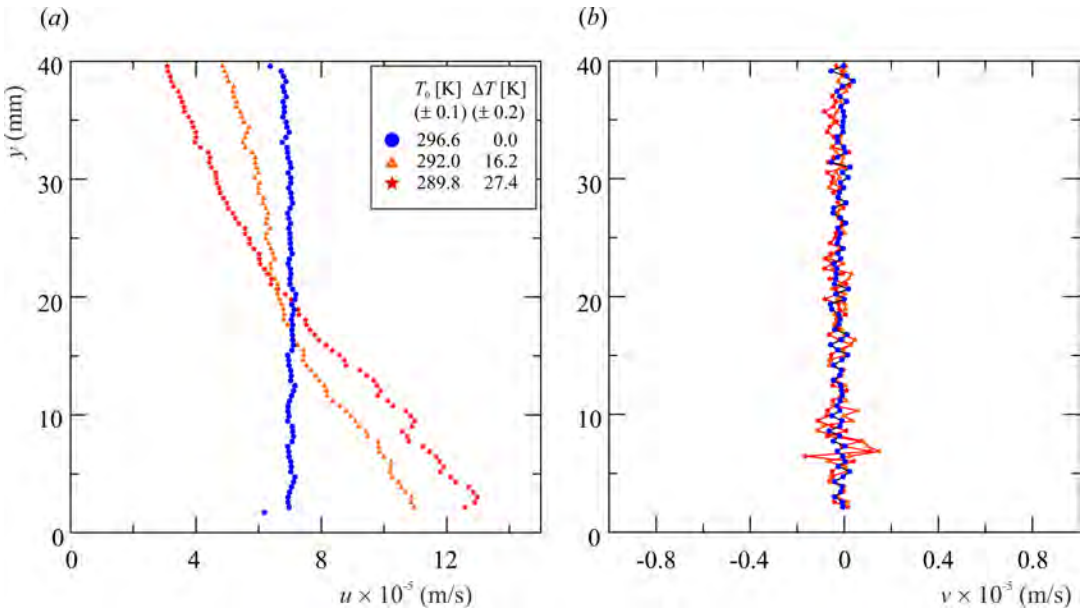

Figure 8: Experimental basic flow with average horizontal velocity 0.007 $\mathrm{cm\,s^{-1}}$. (a) Horizontal velocity corresponding to three different values of ΔT, and (b) vertical velocity. The fluid is a mixture of water, CMC (1.5% wgt), tracers, with $n = 0.88$, $\mu_0^* = 0.72\,\mathrm{Pa\,s}^n$.

Finally, it was difficult to find natural or artificial fluids showing a stable shear-thickening behaviour at the time scales of the present experiments. Most, if not all, shear-thickening fluids are suspensions (see, e.g., cornstarch in water adopted by Longo et al., 2015a, Longo et al., 2015b) and are subject to segregation of the dispersed phase. The time scale of segregation is much smaller than the time scale of the instability process, hence the mixture loosens or at least significantly changes its rheological characteristics during the experiment. This phenomenon is more evident if there are density variations in the mixture induced, e.g., by a spatial temperature gradient. Hence, these mixtures can be used only for relatively fast experiments.

The basic velocity profile has been experimentally verified. Equations (8) and (20) show that, for every value of n, the profile is a linear function of y. In terms of dimensional variables, it is expressed as

$$u_b(y) = u_b(H)\left[1 + \xi\,\Delta T\left(1 - \frac{y}{H}\right)\right]. \tag{25}$$

Figure 8 shows the average horizontal and vertical velocity profiles for the basic flow either with absence of heat flux ($\Delta T = 0\,\mathrm{K}$), within the experimental uncertainty, or with two non-zero temperature differences, $\Delta T = 16.2\,\mathrm{K}$ and $27.4\,\mathrm{K}$. A reasonably linear profile of the horizontal velocity is observed in all three cases, presumably distorted by a small thermal flux at the walls of the cell which causes a deviation of the temperature profile from linearity. The vertical velocity profiles are fluctuating around zero as expected, with larger fluctuations near the bottom where sedimentation is more evident. We estimated the coefficient $\xi = 0.095\,\mathrm{K}^{-1}$.

During the setup and calibration of the experimental apparatus, it become clear that the Hele-Shaw cell can be used, with good accuracy, for the direct measurement of the rheological parameters of the power-law fluid. The details of the method are illustrated in Appendix A.

5 Conclusions and future work

We presented a theoretical formulation for the onset of thermally driven convection in a 2-D porous medium heated from below. The fluid saturating the medium is described by a power-law rheological model. The apparent viscosity is considered as temperature dependent according to a model where the consistency index is variable and the power-law index is constant. The upper boundary is assumed to be open, while the lower boundary is impermeable. The basic horizontal flow across the layer has been determined analytically. A two-dimensional linear stability analysis has been carried out to assess the critical conditions for the onset of convective cells within the layer. The numerical solution of the stability eigenvalue problem has allowed the determination of neutral stability curves for different assignments of the Péclet number, Pe, the variable viscosity parameter, γ, and the power-law index, n. These curves have been plotted in the (α, λ) plane, where α is the perturbation wave number and λ is the ratio between the Rayleigh number, Ra, and Pe^{n-1}. The critical condition, $(\alpha_{cr}, \lambda_{cr})$, is one identifying the minimum of λ (or Ra) along each neutral stability curve. The most important results obtained by the linear stability analysis are the following:

- The Péclet number influences significantly the critical values $(\alpha_{cr}, \lambda_{cr})$ only when γ is large enough. The limiting case of a temperature-independent viscosity ($\gamma \to 0$) is one where $(\alpha_{cr}, \lambda_{cr})$ does not depend on Pe. The same conclusion was drawn by Barletta and Nield (2011) for the case of a porous layer with impermeable boundaries.

- There is a generally destabilising effect of the variable viscosity, namely the critical value of λ decreases with γ, for fixed n and Pe. This behaviour has been previously documented in the literature for the case $n = 1$ where both the lower and the upper boundaries are impermeable (Kassoy and Zebib, 1975; Nield, 1996).

- When Pe and/or γ are large enough, the usual upward concave shape of the neutral stability curve turns into a double minimum shape. This results into a discontinuity of α_{cr} when plotted versus γ.

As the experimental study of Rayleigh-Bénard convection of non-Newtonian fluids in two-dimensional porous media with an open boundary is a relatively new endeavour, an Hele-Shaw cell was built from scratch to test the theoretical formulation. Some preliminary tests were conducted, showing the appearance and development of recirculation cells as the temperature gradient across the cell increases. The horizontal velocity profile corresponding to the basic flow was reproduced accurately. These experimental results, in qualitative agreement with the theory, highlighted instability for zero transverse flow, and strong hysteretic effects: the cells, once formed, continued to exist even if the temperature gradient was decreased well below the value it had on their first detection. These effects, associated to nonlinearity, need to be quantified to determine the approximation associated with the linear stability analysis.

Furthermore, the experimental setup allowed to identify several issues of relevance in the planning of a comprehensive set of experiments geared at verifying the theory. Firstly, the order of magnitude of the velocity field to be measured (millimeters per second) requires accurate measurements. Secondly, the rheometry of the fluid proves to be essential in interpreting the flow behaviour, as deviations from

power-law behaviour at small shear rates may contribute to instabilities. The need to measure the fluid parameters in the appropriate range of shear rates is confirmed. To this end, it was demonstrated that the Hele-Shaw cell can be used for the direct measurement of the rheological parameters of the power-law fluid. Thirdly, an appropriate selection of tracers is crucial for accurate measurements: good results are obtained when the tracer density is close to the fluid's. Pine pollen particles, used in the preliminary tests, could be substituted with microsponges in future experiments. Fourthly, experimental verification of the behaviour of shear-thickening fluids proves difficult, as most suspensions tend to segregate fairly quickly, changing significantly their characteristics during the experiment. Hence, tests with these mixtures should be limited to relatively fast experiments. While the boundary condition with a a rigid lid can be easily reproduced, the free surface boundary condition requires additional efforts: the need of a non-zero flow in the cell forces a space pressure gradient which can be achieved only by tilting the cell. In order to avoid contact with the aluminium shim, the angle of tilting should be equal to the free surface inclination. This may prove difficult, since the free surface inclination is readily variable following different dissipation regimes of the current, which in turn depend on the average fluid temperature. In addition, the air cushion between the shim and the free surface has a low thermal conductivity, hence there is a significant temperature difference between the horizontal upper frame and the fluid. This makes the evaluation of the temperature gradient uncertain.

The study carried out in this paper opens significant perspectives for future work. The following aspects need to be further developed:

(i) The linear stability analysis can be expanded in order to include boundary conditions closer to those actually implemented in the experimental setup. Also the model of temperature-dependent viscosity can be adapted to the actual rheological behaviour of the working fluid employed in the experiment.

(ii) A comprehensive set of experiments is to be planned and implemented. The aim is obtaining the values of λ that identify the threshold for the onset of thermally driven convection, and the associated uncertainty. Also an adaptation of shadowgraphic methods can be tested to indirectly detect the density fluctuations associated with the incipient development of the cells.

(iii) A crucial aspect to be further developed is the modelling of the non-Newtonian behaviour when $Pe \to 0$. This point was discussed in Nield (2011a). This author suggested that the power-law behaviour should turn into an effectively Newtonian behaviour when $Pe \to 0$. The importance of extensive experiments in this regime can be very important to establish whether the onset convection depends or not on n when Pe is vanishingly small.

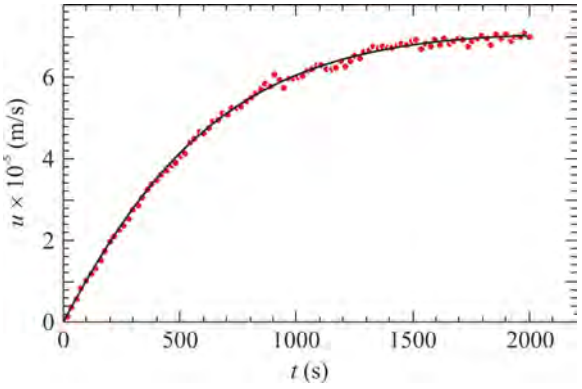

Figure A.1: Time series of the average velocity measured during unsteady-state flow in the Hele-Shaw cell. The fluid is a mixture of water, CMC (1.5% wgt), tracers, $T_0 = 296.3\,\mathrm{K}$, the same used for the experiments shown in Figure 7. The bold line indicates the theoretical velocity according to eq. (A.1), with the fitted parameters $n = 0.88$, $\mu_0^* = 0.72\,\mathrm{Pa\,s}^n$, $Q = 0.0169\ \mathrm{cm}^3\,\mathrm{s}^{-1}$.

Appendix A Measuring the fluid rheological parameters by the Hele-Shaw cell

A major issue in analyzing the rheological behaviour of non-Newtonian fluids is the correct estimation of rheometric parameters. As the two-parameter power-law model is an approximation of more complex models (e.g., the four-parameter Cross or Carreau-Yasuda model), the estimation of its rheometric parameters is strongly related to the expected interval of shear rate values. Hence the first step is usually an estimation of the expected shear rate in the experiments, which is often based on a model of the flow field (see, e.g., Longo et al. (2013)) and subject to uncertainty. In addition, the geometry of the rheometer itself affects the results: for a power-law fluid, a parallel plate rheometer gives different values of the fluid behaviour and consistency indexes with respect to the values obtained with a cup and bob rheometer. In order to partially overcome all these approximations, we tested the feasibility of a direct measurement of the power-law parameters in the Hele-Shaw cell. To this aim, the syringe pump was used to inject the fluid at a constant influx rate in one of the well of the Hele-Shaw cell, which was already filled with the same fluid. The PIV system monitored the average horizontal velocity of the fluid in the cell. The fluid started to flow in the other well, which serves as an accumulator. The process is described by the following equation:

$$\frac{L}{g}u^{1-n}\frac{d^2u}{dt^2} + \frac{L\mu_0^*}{\rho g}\left(\frac{2}{b}\right)^{n+1}\left(\frac{2n+1}{n}\right)^n n\frac{du}{dt} + \left(\frac{bh}{A_1}+\frac{bh}{A_2}\right)u^{2-n} = \frac{Q(t)}{A_1}u^{1-n}, \tag{A.1}$$

where u is the average horizontal velocity of the fluid in the cell, L is the cell length, g is gravity, μ_0^* and n are the consistency and fluid behaviour indexes of the fluid, b and h are the cell gap and height, respectively, A_1 and A_2 are the cross-section areas of the upstream and downstream wells, respectively, and Q is the influx rate. We have assumed no outflow. After imposing a constant influx rate Q, PIV measurements generated the time series of average velocity u. The unknowns are μ_0^* and n, which are estimated by an optimization procedure of the parametric differential equation (A.1).

Figure A.1 shows the experimental points and the theoretical velocity (bold line) estimated with the optimization procedure. The fluid is identical to that used for the experiments shown in Figure 7. The differences between the rheological parameters measured with the parallel plate rheometers ($n = 0.9$ and $\mu_0^* = 0.25\ \mathrm{Pa\,s}^n$) and with the new methodology ($n = 0.88$, $\mu_0^* = 0.72\,\mathrm{Pa\,s}^n$), can be attributed to the different flow field generated in the rheometer and in the Hele-Shaw cell and to the different average shear rate. Note that the influx rate Q can be either known or estimated by the velocity measurements, but in the former case the overall uncertainty increases. For constant influx rate, the asymptotic average velocity in the cell is equal to

$$u_\infty = \frac{Q}{bh(1 + A_1/A_2)}. \tag{A.2}$$

References

Alloui, Z. Z., Khelifa, N., Beji, H. H., Vasseur, P. P., Onset of convection in a horizontal porous layer saturated by a power-law fluid. ASME Journal of Heat Transfer, **134**, 092502 (2012).

Alves, L. S. B., Barletta, A., Convective instability of the Darcy-Bénard problem with through flow in a porous layer saturated by a power-law fluid. International Journal of Heat and Mass Transfer, **62**, 495–506 (2013).

Barletta, A., Thermal instability in a horizontal porous channel with horizontal through flow and symmetric wall heat fluxes. Transport in Porous Media, **92**, 419–437 (2012).

Barletta, A., Celli, M., Kuznetsov, A. V., Nield, D. A., Unstable forced convection in a plane porous channel with variable-viscosity dissipation. ASME Journal of Heat Transfer, **138**, 032601 (2016).

Barletta, A., Nield, D. A., Linear instability of the horizontal throughflow in a plane porous layer saturated by a power-law fluid. Physics of Fluids, **23**, 013102 (2011).

Barletta, A., Nield, D. A., Variable viscosity effects on the dissipation instability in a porous layer with horizontal throughflow. Physics of Fluids, **24**, 104102 (2012).

Barletta, A., Storesletten, L., Linear instability of the vertical throughflow in a horizontal porous layer saturated by a power-law fluid. International Journal of Heat and Mass Transfer, **99**, 293–302 (2016).

Buretta, R. J., Berman, A. S., Convective heat transfer in a liquid saturated porous layer. Journal of Applied Mechanics, **43**, 249–253 (1976).

Cherkaoui, A. S. M., Wilcock, W. S. D., Laboratory studies of high Rayleigh number circulation in an open-top Hele-Shaw cell: An analog to mid-ocean ridge hydrothermal systems. Journal of Geophysical Research: Solid Earth, **106**, 10983–11000 (2001).

Darbouli, M., Métivier, C., Piau, J.-M., Magnin, A., Abdelali, A., Rayleigh-Bénard convection for viscoplastic fluids. Physics of Fluids, **25**, 023101 (2013).

Delenda, N., Hirata, S. C., Ouarzazi, M. N., Primary and secondary instabilities of viscoelastic mixtures saturating a porous medium: Application to separation of species. Journal of Non-Newtonian Fluid Mechanics, **181-182**, 11–21 (2012).

Hartline, B. K., Lister, C. R. B., Thermal convection in a Hele-Shaw cell. Journal of Fluid Mechanics, **79**, 379–389 (1977).

Hirata, S. C., Ouarzazi, M. N., Three-dimensional absolute and convective instabilities in mixed convection of a viscoelastic fluid through a porous medium. Physics Letters A, **374**, 2661–2666 (2010).

Horton, C. W., Rogers, F. T., Convection currents in a porous medium. Journal of Applied Physics, **16**, 367–370 (1945).

Howle, L., Behringer, R., Georgiadis, J., Convection and flow in porous media. Part 2. Visualization by shadowgraph. Journal of Fluid Mechanics, **332**, 247–262 (1997).

Kaity, S., Maiti, S., Ghosh, A., Pal, D., Ghosh, A., Banerjee, S., Microsponges: A novel strategy for drug delivery system. Journal of Advanced Pharmaceutical Technology & Research, **1**, 283–290 (2010).

Kassoy, D. R., Zebib, A., Variable viscosity effects on the onset of convection in porous media. Physics of Fluids, **18**, 1649–1651 (1975).

Keene, D. J., Goldstein, R., Thermal convection in porous media at high Rayleigh numbers. Journal of Heat Transfer, **137**, 034503 (2015).

Lapwood, E. R., Convection of a fluid in a porous medium. Proceedings of the Cambridge Philosophical Society, **44**, 508–521 (1948).

Letelier, J. A., Herrera, P., Mujica, N., Ortega, J. H., Enhancement of synthetic schlieren image resolution using total variation optical flow: application to thermal experiments in a Hele-Shaw cell. Experiments in Fluids, **57**, 1–14 (2016).

Lister, C., An explanation for the multivalued heat transport found experimentally for convection in a porous medium. Journal of Fluid Mechanics, **214**, 287–320 (1990).

Longo, S., Di Federico, V., Chiapponi, L., Non-Newtonian power-law gravity currents propagating in confining boundaries. Environmental Fluid Mechanics, **15**, 515–535 (2015a).

Longo, S., Di Federico, V., Chiapponi, L., Propagation of viscous gravity currents inside confining boundaries: the effects of fluid rheology and channel geometry. Proceedings of the Royal Society of London A: Mathematical, Physical and Engineering Sciences, **471**, 20150070 (2015b).

Longo, S., Di Federico, V., Chiapponi, L., Archetti, R., Experimental verification of power-law non-Newtonian axisymmetric porous gravity currents. Journal of Fluid Mechanics, **731**, R2 (2013).

Nield, D. A., Onset of thermohaline convection in a porous medium. Water Resources Research, **11**, 553–560 (1968).

Nield, D. A., The effect of temperature-dependent viscosity on the onset of convection in a saturated porous medium. Journal of Heat Transfer, **118**, 803–805 (1996).

Nield, D. A., A note on the onset of convection in a layer of a porous medium saturated by a non-Newtonian nanofluid of power-law type. Transport in Porous Media, **87**, 121–123 (2011a).

Nield, D. A., A further note on the onset of convection in a layer of a porous medium saturated by a non-Newtonian fluid of power-law type. Transport in Porous Media, **88**, 187–191 (2011b).

Nield, D. A., Bejan, A., Convection in Porous Media, 4th edition. Springer-Verlag, New York (2013).

Nowak, Z., Gryglaszewski, P., Stacharska-Targosz, J., Laminar heat transfer to power law fluids in flat gaps with various thermal wall conditions. Acta Mechanica, **44**, 223–236 (1982).

Prats, M., The effect of horizontal fluid flow on thermally induced convection currents in porous mediums. Journal of Geophysical Research, **71**, 4835–4838 (1966).

Rees, D. A. S., The stability of Darcy–Bénard convection. In Vafai, K., Hadim, H. A., editors, Handbook of Porous Media, chapter 12, pages 521–558. CRC Press, New York (2000).

Rees, D. A. S., Convection of a Bingham fluid in a porous medium. In Vafai, K., editor, Handbook of Porous Media, chapter 17, pages 559–595. CRC Press, third edition (2015).

Sveen, J. K., An Introduction to MatPIV v. 1.6.1. Dept. of Math., University of Oslo (2004).